Mitochondrion 70 (2023) 20–30

Contents lists available at ScienceDirect

Mitochondrion

journal homepage: www.elsevier.com/locate/mito

Augmented *Parkin*-dependent mitophagy underlies the hepatoprotective effect of remote ischemic conditioning used prior to hemorrhagic shock

Avinash Naraiah Mukkala [a,b], Raluca Petrut [a], Rachel Goldfarb [a], Erika Leigh Beroncal [c], Chung Ho Leung [a,b], Zahra Khan [a,b], Menachem Ailenberg [a], Mirjana Jerkic [a], Ana C. Andreazza [c], Shawn G. Rhind [d], Marc G. Jeschke [e], Andras Kapus [a,b,f,g], Ori D. Rotstein [a,b,f,*]

[a] Keenan Research Centre for Biomedical Science, St. Michael's Hospital, Toronto, Canada
[b] Institute of Medical Science, University of Toronto, Toronto, Canada
[c] Department of Pharmacology & Toxicology, University of Toronto, Toronto, Canada
[d] Defence Research and Development Canada, Department of National Defense, Government of Canada, Toronto, Canada
[e] Hamilton Health Sciences Centre and McMaster University, Hamilton, Canada
[f] Department of Surgery, University of Toronto, Toronto, Canada
[g] Department of Biochemistry, University of Toronto, Toronto, Canada

ARTICLE INFO

Keywords:
Mitochondria
Parkin-dependent mitophagy
Mitochondrial quality control
Ischemia–reperfusion injury
Hemorrhagic shock-resuscitation

ABSTRACT

Background and aims: Hemorrhagic shock-resuscitation (HSR) following trauma contributes to organ dysfunction by causing ischemia–reperfusion injury (IRI). We previously showed that 'remote ischemic preconditioning' (RIPC) exerted multi-organ protection from IRI. Maintenance of mitochondrial quality by clearance of dysfunctional mitochondria via mitophagy is vital in restoring organ integrity. We hypothesized that *parkin*-dependent mitophagy played a role in RIPC-induced hepatoprotection following HSR.
Methods: The hepatoprotective effect of RIPC in a murine model of HSR-IRI was investigated in wild type and *parkin*-/- animals. Mice were subjected to HSR ± RIPC and blood and organs were collected, followed by cytokine ELISAs, histology, qPCR, Western blots, and transmission electron microscopy.
Results: HSR increased hepatocellular injury, as measured by plasma ALT and liver necrosis, while antecedent RIPC prevented this injury; in *parkin*$^{-/-}$ mice, RIPC failed to exert hepatoprotection. The ability of RIPC to lessen HSR-induced rises in plasma IL-6 and TNFα, was lost in *parkin*$^{-/-}$ mice. While RIPC alone did not induce mitophagy, the application of RIPC prior to HSR caused a synergistic increase in mitophagy, this increase was not observed in *parkin*$^{-/-}$ mice. RIPC induced shifts in mitochondrial morphology favoring mitophagy in WT but not in *parkin*$^{-/-}$ animals.
Conclusions: RIPC was hepatoprotective in WT mice following HSR but not in *parkin*$^{-/-}$ mice. Loss of protection in *parkin*$^{-/-}$ mice corresponded with the failure of RIPC plus HSR to upregulate the mitophagic process. Improving mitochondrial quality by modulating mitophagy, may prove to be an attractive therapeutic target in disease processes caused by IRI.

1. Introduction

Resuscitated hemorrhagic shock (HSR) following major trauma can contribute to multiple organ dysfunction through the induction of ischemia–reperfusion injury (IRI) (Davidson et al., 2011; Regel et al., 1996). The pathophysiology of IRI and the role of oxidative stress are well-studied (Wu et al., 2018; Kalogeris et al., 2012). Post-HSR hepatic IRI induces mitochondrial perturbation leading to membrane depolarization, oxidative phosphorylation uncoupling, and ATP depletion, which all contribute to cell/tissue death (Kim et al., 2003, 2007; Go et al., 2015), either directly or through the initiation of various cellular cascades that lead to inflammation and injury. Restoration of mitochondrial quality, through mitochondrial biogenesis and active clearance of dysfunctional mitochondria—an autophagic process termed 'mitophagy'—are considered crucial for re-establishing cellular homeostasis in response to injury (Kim et al., 2003, 2007; Go et al., 2015).

* Corresponding author at: 209 Victoria Street, Toronto, ON M5B 1T8, Canada.
E-mail address: Ori.Rotstein@unityhealth.to (O.D. Rotstein).

https://doi.org/10.1016/j.mito.2023.03.002
Received 23 October 2022; Received in revised form 4 February 2023; Accepted 5 March 2023
Available online 10 March 2023

Remote ischemic preconditioning (RIPC)—cycles of transient limb occlusion and release has been shown to be protective in IRI, in experimental models as well as in humans (Lim and Hausenloy, 2012). In humans, RIPC has been shown to exert protection in: abdominal aortic aneurysm repair (Li et al., 2013), acute ischemic stroke (Hougaard et al., 2013), contrast-induced nephropathy (Koch et al., 2016), congenital heart disease (Lim and Hausenloy, 2012; Cheung et al., 2006), and coronary artery bypass surgery (Lim and Hausenloy, 2012). In the experimental setting, the role of RIPC protection has been explored in models of liver IRI. For example, Kim and colleagues demonstrated that RIPC was able to exert protection against liver IRI through the induction of autophagy (Wang et al., 2014). In a murine model of HSR, our group showed previously that liver inflammation and injury were reduced by RIPC in an Nrf2-dependent fashion and this protection correlated with a rise in autophagy/mitophagy. In other models of IRI, various groups have shown that autophagy/mitophagy can be protective (Kong et al., 2021; Leung et al., 2018; Li et al., 2018; Livingston et al., 2019; Zhang et al., 2021). For example, Huang *et al.* implicated *Parkin* and p62 in IPC-induced selective mitophagy related to protection following cardiac ischemia/reperfusion (Huang et al., 2011). In addition, Livingston *et al.* have shown that mitophagy is central in the protection afforded by IPC in renal IRI (Livingston et al., 2019). Other reports have suggested that preconditioning might positively impact mitochondrial function in cardiac systems (Quarrie et al., 2012; Slagsvold et al., 2014), for example by inhibiting mitochondrial permeability transition pore (mPTP) opening (Turrell et al., 2014; Zheng et al., 2014).

The mechanisms whereby RIPC can exert *remote* organ protection contain knowledge gaps requiring attention. While the possible contribution of mitophagy to organ protection related to RIPC has been suggested, their causal relationship has not been clarified and the underlying mechanisms remain to be elucidated. *Parkin* is a cytosolic E3 ubiquitin ligase which is recruited to serine/threonine protein kinase PINK on the surface of mitochondria under conditions of mitochondrial/oxidative stress and together these proteins initiate sequential ubiquitination of mitochondrial proteins, thereby decorating dysfunctional mitochondria for their clearance by mitophagic processes. The PINK1/*Parkin* pathway is recognized to be a key effector of mitophagy (i.e., mitochondrial macroautophagy). *Parkin* has also been explored in the context of liver, cardiac and renal IRI, and been implicated in the preconditioning mechanism (Kong et al., 2021; Huang et al., 2011; Gu et al., 2020; Zhu et al., 2020). Given our previous demonstration that RIPC-induction of autophagy/mitophagy correlated with the hepatocellular protection exerted by RIPC applied prior to HSR, we hypothesized that RIPC may exert its beneficial effects in murine HSR through the initiation of mitophagy in a *Parkin*-dependent manner.

2. Methods

2.1. Animal ethics, housing, and knock-out breeding

All animal studies were conducted in compliance with the Animal Care Committee (ACC) at St. Michael's Hospital (Toronto, Canada – ACC #857). Mice (7-12w, n = 44, 22 wt and 22 *parkin*$^{-/-}$) were all housed in pairs, with continual access to water and food, on a 12 h day-night light cycle. *Parkin* knock-out (*parkin*$^{-/-}$) mice (*Park2*^{tm1Shn}) were acquired, and a male-only breeding colony was maintained in the vivarium breeding program at the Keenan Research Centre for Biomedical Science (JAX stock #006582) (Goldberg et al., 2003). The *parkin*$^{-/-}$ mice are viable and fertile, and lack full length protein due to an exon 3 mutation that results in a frame shift to facilitate a premature stop codon in exon 5. Wild-type (WT) mice were of the same C57BL/6J genetic background (JAX stock #000664). Wild-type animals are referred to as *parkin*$^{+/+}$ in figures throughout. The *parkin*$^{-/-}$ mice are of the same genetic background as the WT controls and are specific knockout for the *PRKN2* gene. Mice were permitted at least one week of acclimatization to the vivarium facility before surgery.

2.2. Parkin knock-out genotyping and protein expression

DNA was extracted from ear notch tissue (REDExtract N-Amp Tissue PCR Kit, Sigma-Aldrich). Knockout (KO) and WT DNA samples were PCR amplified (Veriti Thermocycler, Applied Biosystems). Primers for KO genotyping are provided in Supplementary Table 1 (Zhu et al., 2020). PCR product was run on a 1.5% ultrapure agarose gel at 100 V for 30mins and imaged on the GelDoc EZ Imager (Bio-Rad) (Supplementary Fig. 1A). Images were analyzed in Image Lab software (v6.0.1, Bio-Rad). Loss of full-length *Parkin* protein expression was confirmed using the Western blot protocol described below (Fig. 5A and 5C; Supplementary Fig. 1B). Recently, (Mekada and Yoshiki, 2021) describe a mutation in the nicotinamide nucleotide transhydrogenase (NNT) gene of C57BL/6J wild-type mice (Mekada and Yoshiki, 2021). Given that C57BL/6J mice are widely used as controls in IRI studies, and that our knockout *parkin*$^{-/-}$ (also obtained from Jackson Laboratories) mice are of the same genetic background, we opted to use these mice as the experimental design mitigates any effect that the NNT mutation may have (Mekada and Yoshiki, 2021).

2.3. In vivo murine hemorrhagic shock-resuscitation model

HSR was performed using previously described methods; the mouse model is a pressure-controlled hypovolemic shock model (Leung et al., 2018, 2015). Briefly, male WT C57BL/6J and *parkin*$^{-/-}$ mice (Jackson Laboratories, Bar Harbor, ME) (9–12w, 25 ± 2.06 g) were anesthetized via intraperitoneal injection of sodium pentobarbital (70 mg/kg) (euthanyl, Bimeda-MTC Animal Health Inc., Cambridge, ON) and allowed to rest for 15 min before first incision. We opted to use pentobarbital as our anesthetic, as it is commonly used in IRI and HSR mouse models due to its minimal effect on mouse hemodynamics. We opted to not use isoflurane as it has previously been shown to be a preconditioning agent in IRI models (Chen et al., 2008). All animal groups in this study received pentobarbital. Animals were placed on a warming pad throughout the procedure with constant temperature monitoring through a rectal thermometer lubricated with 100% white petroleum (Type K Thermometer, Fischer Scientific). Under 20-40X microscopic examination, microvascular cannulation of the right carotid and left hindlimb femoral arteries were achieved with stretched polyethylene tubing (BD Intramedic, PE10 #427401) infused with sterile heparin-saline solution (10U/mL, Fresenius Kabi, Toronto, ON). During this cannulation surgery, RIPC was performed using a tourniquet around the right hindlimb, intermittently for 4 cycles of 5-mins each of occlusion and release. Incision sites were both subcutaneously injected with 50uL of 0.05% bupivacaine hydrochloride-saline for local analgesia (SteriMax, Oakville, ON). Mean arterial pressure (MAP) was constantly monitored using the carotid cannula connected to a pressure transducer (DTXPlus, DT-XX, #682018) and physiologic monitor (PM-9000Vet, Mindray Biomedical Technologies) (Fig. 1A). MAP was brought down to 30 mmHg by controlled hemorrhage from the femoral cannula over a 30 min stabilization period and maintained for two more hours. Mice were resuscitated using all shed blood and Lactated Ringer's Solution equal to two volumes shed blood, over 15 mins. 2 h after resuscitation, animals were sacrificed; blood was collected, and organs were flash frozen in liquid nitrogen. Animals were maintained in surgical plane with sodium pentobarbital as required (70 mg/kg).

2.4. Transmission electron microscopy sample processing and imaging

Liver tissue was cut into 1–2 mm^3 and immersed in primary fixative (4% Paraformaldehyde plus 1% Glutaraldehyde in 0.1 M phosphate buffer, pH = 7.2) for at least 24 h at 4 °C. Tissues were then postfixed in secondary fixative (1% Osmium Tetraoxide buffered with 0.1 M Phosphate, pH = 7.2) for at least 1 h at room temperature and dehydrated in an ethanol series over 3 h. Finally, tissues were embedded in Epon resin and polymerized at 40 °C for 48 h. Ultrathin 100 nm sections were cut,

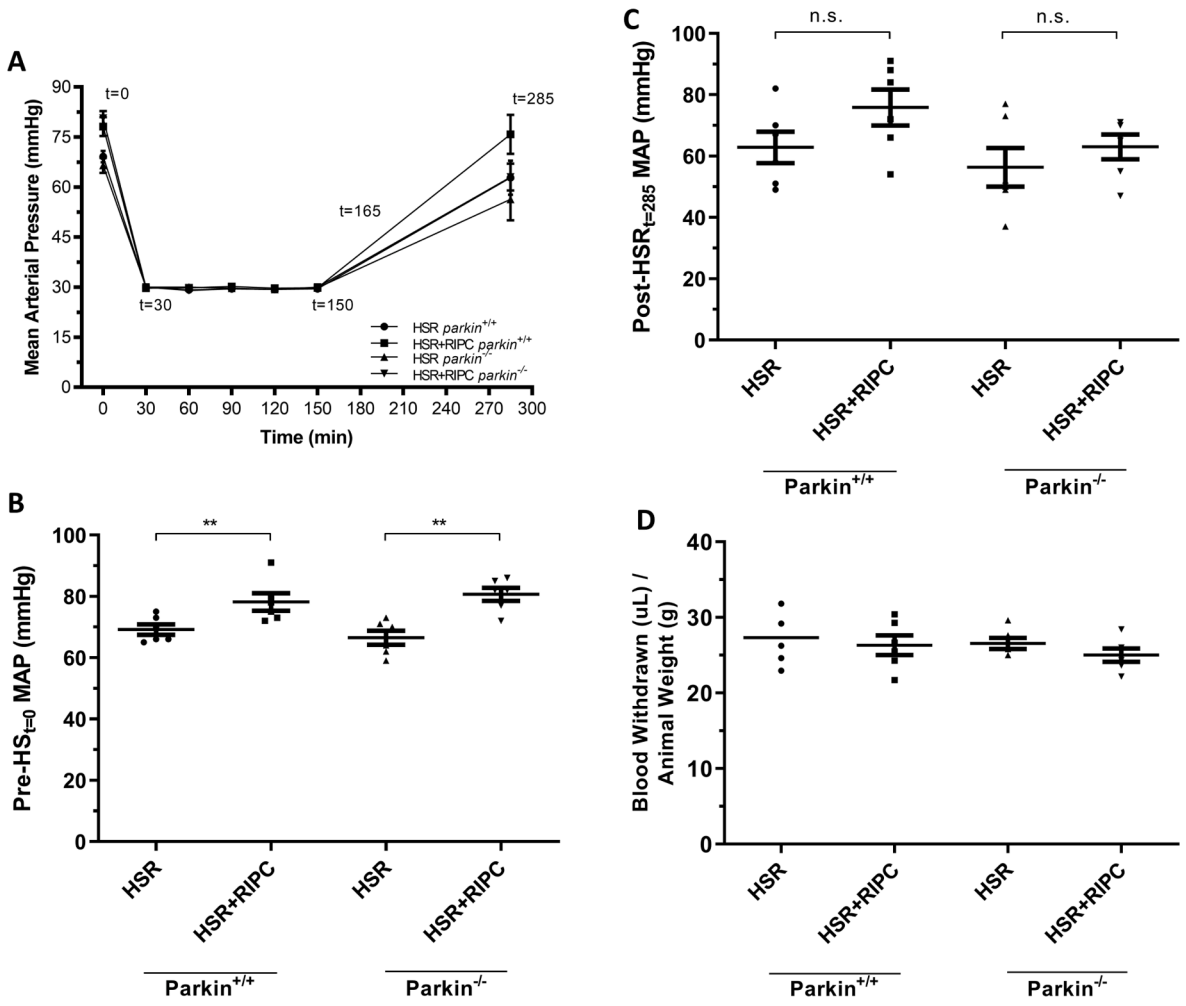

Fig. 1. Hemodynamics in murine *in vivo* hemorrhagic/resuscitation. *(A)* Hemorrhagic shock/resuscitation model mean arterial pressure (MAP) profile for all animals included in study (n = 44). *(B-C)* Pre-shock (t = 0 min) MAP showed a transient but significant increase in MAP in RIPC animals, which did not persist post-shock (t = 285 min). *(D)* Blood withdrawn per gram weight of an animal was used as a standard model validation parameter (n = 5–6 per group). **p < 0.01. n.s. = not significant.

and contrast stained with 5% uranyl acetate and Reynold's lead citrate. Samples were examined utilizing the Talos L120C transmission electron microscope (TEM) system, and 10–15 random images per sample were captured with the high resolution 4 K × 4 K CETA CMOS camera (ThermoFischer Scientific).

2.5. Ultrastructural mitochondrial morphology analysis

Examining previously established definitions/methods (Mollica et al., 2017; Solenski et al., 2002; Dong et al., 2006; De Gaetano et al., 2020; Das et al., 2012; Mortiboys et al., 2008; Grünewald et al., 2010; Lucocq and Hacker, 2013; Garvin et al., 2017; Velez et al., 2016; Yu et al., 2016; Lutz et al., 2009; Pinto et al., 2018; Westermann, 2012; Kalkhoran et al., 2017; Khraiwesh et al., 2013; Redmann et al., 2018; Reis-Barbosa et al., 2020; Westrate et al., 2014; Coronado et al., 2018), and the fact that unstimulated hepatic mitochondria show fairly slow dynamics (Das et al., 2012), and the spheroid-ovoid nature of liver mitochondria (Youle and van der Bliek, 2012), a blinded image analysis was setup. Images were contrast-adjusted in MAPS TIA Software (ThermoFischer Scientific), and morphometric measurements and counting were conducted in ImageJ with the TIA Reader Plugin (v.1.8.0_112, 2015). All images were assessed by a blinded observer (RG). Mitophagophores were defined as mitochondria with partially formed double membranes around them, mitophagosomes were defined as mitochondria with fully formed double membranes around them, and amorphous calcium-phosphate (CaP) granulated mitochondria were defined as being darker than surrounding mitochondria and having electron-dense dots within the mitochondria. The total number of mitophagosomes and mitophagophores per five 100 μm^2 fields per sample were counted. The number of mitochondria that displayed calcium-phosphate granulation were counted per ten 100 μm^2 fields (Solenski et al., 2002; Dong et al., 2006). We evaluated mitophagophores and mitophagosomes as measures of the early and late stages of mitophagy respectively and the presence of Calcium phosphate granules, indicative of calcium accumulation in damaged mitochondria. For quantitative morphology studies, the total number of mitochondria per 8–10 100 μm^2 fields per mouse liver were counted and each mitochondrion was measured for area, perimeter and ImageJ parameters of aspect ratio, roundness, and circularity. The form factor per mitochondrion, mitochondrial density, and mitochondrial coverage were calculated.

2.6. Liver histology and necrosis quantification

Liver tissue was cut into ~5 mm^3 and fixed by immersion in 10% neutral buffered formalin for 24 h, then washed three times with PBS and resuspended in 70% EtOH until sectioning. Tissue was prepared using an automatic tissue processor (Leica TP1020). Tissue was

embedded in paraffin wax (Leica EG1160), cut into 5um sections (Leica RM2235) and auto-stained with hematoxylin and eosin (Leica Autostainer XL). Coverslips were placed using toluene (Permount, Fischer Chemical). Using the Zeiss Axio Scan (v2.1) system, images of entire slides were captured and analyzed in ZEN (v3.1). Confluent necrosis was defined by areas of the liver that had a marked lighter pink (rather than darker purple) staining; these areas often present with hepatocellular congestion and cytoplasmic vacuolization. The total necrosis area percentage per liver section was quantified using a blinded observer by tracing the necrotic region and dividing by the total area of the liver slice (Leung et al., 2018).

2.7. Western blots

Liver tissues were agitated and homogenized using mortar and pestle in lysis buffer containing: 10 mM NaCl, 30 mM HEPES, 20 mM NaF, 1 mM EGTA, 1% Triton X, 1 mM sodium orthovanadate, and complete protease inhibitor cocktail (Roche Diagnostics, Mannheim, Germany). After centrifugation at 12,000 RPM (13,800*g*) for 10 min at 4 °C, the supernatant was collected and aliquoted for storage at −80 °C until use. Protein concentrations were determined by Bio-Rad DC Protein Assay (Bio-Rad, Hercules, CA). 40ug of protein sample was loaded onto 10%, 12% or 15% sodium dodecyl sulfate–polyacrylamide gel electrophoresis (SDS-PAGE), and electrophoretic transfer was performed onto nitrocellulose or polyvinylidene fluoride membranes (Bio-Rad). Membranes were blocked on a rocking platform for 1 h at room temperature in 5% skim milk in tris-buffered saline Tween 20 (TBST). Membranes were probed with primary antibodies (*Parkin2*, 1:800, Santa Cruz #32282; PINK1, 1:800, Cell Signaling #6946*S*; p62, 1:1000, Cell Signaling #5114S; GAPDH, 1:40000, Cell Signaling #5174S; BNIP3L/Nix, 1:5000, Cell Signaling #12396; FUNDC1, 1:5000, Cell Signaling, # 49240) diluted in 5% skim milk-TBST and incubated overnight at 4 °C on a rocking platform. After 3 washes in TBST, membranes were incubated with appropriate secondary horseradish peroxidase antibodies (AffiniPure donkey anti-rabbit IgG #711-035-152; AffiniPure goat anti-mouse IgG light chain #115-035-174; Jackson Immuno-Research) for 1 h at room temperature. After 3 more TBST washes, membranes underwent enhanced chemiluminescence (Ultrascence ECL Western Blot Substrate, Frogga Bio) followed by exposure in the ChemiDoc Touch Imaging System (Bio-Rad). Signal bands were normalized to GAPDH per lane. Densitometry volume of signals were quantified in Image Lab software (v6.0.1, Bio-Rad), and normalized to appropriate sham groups.

2.8. qRT-PCR mRNA expression quantification

Liver tissue was weighed, homogenized with mortar and pestle, syringed through a 26-gauge needle, and run through the Qiashredder column (Qiagen) at 21100xg for 2mins. RNA was extracted according to the RNeasy Mini Kit protocol (Qiagen). NanoDrop analysis was performed for RNA purity and concentration (NanoDrop 2000, Thermo Scientific). RNA samples were DNase I treated (EN0525, Thermo Scientific). cDNA was synthesized using the iScript reverse transcriptase (Bio-Rad). qPCR was run using a SYBR green reagent (PowerSYBR Green PCR Master Mix, Applied Biosystems) and 300 nM of primer mix in the QuantStudio 7 system (Applied Biosystems). C_t values were collected and analyzed using $2^{-\Delta\Delta Ct}$ method. Primers are listed in Supplementary Table 1. Primers were validated using an efficiency test, melting curves for specificity and amplicon products run on 1.5% agarose gel.

2.9. mtDNA ND1 and ND4 copy number qPCR quantification

The protocol used for mtDNA copy number was derived from a previously published method by Venegas & Halberg (Venegas and Halberg, 2012), mtDNA copy number was measured through qPCR using 3 primer pairs: (1) β2-Microglobulin (nDNA) (2) ND1 (mtDNA) (3) ND4 (mtDNA) (Supplementary Table 1). Primers were validated by performing a serial dilution of a reference sample: a mixture of 20uL extracted DNA from each tube of available mouse liver samples, to better represent experimental conditions, then running an efficiency test. Along with the efficiency test, a melt curve was generated to confirm the specificity of each primer. β2-Microglobulin was used as a control for variations in starting DNA quantity as it is a one-copy gene with the nuclear genome. DNA was extracted from frozen mouse liver tissues via an in-house DNA extraction protocol which used proteinase-K digestion. The extracted DNA was diluted to a concentration of 0.1 ng/uL and plated with Bioline 2X SensiFAST SYBR No-Rox (Catalog No: #BIO-98050). The qPCR was performed using Bio-Rad CFX96 (Bio-Rad Laboratories Inc.) with the following cycling conditions: 95C for 3 min, 95C for 10 s, 60C for 20 s, repeated for 40 cycles. Following completion of qPCR, ΔCt was calculated for each sample (ΔCt= (average mtDNA Ct) – (average nDNA Ct)), from which mtDNA copy number was calculated (mtDNA copy number = $2^*(2^{-\Delta Ct})$.

2.10. Plasma ALT

Fresh mouse blood was centrifuged (Sorvall Legend Micro 21R, Thermo Scientific) at 2500*g* for 10mins at 4 °C, and plasma supernatant was collected. ALT concentration was quantified within 24 h by the St. Michael's Hospital Diagnostic Laboratory (Toronto, ON).

2.11. Enzyme-linked immunosorbent assays

Plasma samples were stored at −80 °C until usage. ELISA kits were used to measure the concentration of TNF-α, IL-6, and IL-10 in plasma samples (Mouse IL-6 Quantikine ELISA Kit M6000B, Mouse TNF-α Quantikine ELISA Kit MTA00B, Mouse IL-10 Quantikine ELISA Kit (M1000B; R&D Systems).

2.12. Data analysis and statistics

All animal data were anonymized, prior to any type of statistical analyses or sample handling. GraphPad Prism (version 8.2) and R-Studio Desktop 1.3.1073 (R version 4.0.2; 2020-06-22) were used for all data visualization and statistical analysis. The following R packages and functions were used: res.aov and TukeyHSD for statistics and dpylr, ggplot2, and geom_violin for data visualization and statistics. The TEM morphometric dataset was tested for normality in R to check for homogeneity of variances and plots of residuals (Q-Q plots and residual plots). Morphometric data was $\log_{10}$ transformed for visualization and analysis, as required. ANOVA with Tukey's HSD test was conducted for testing significance between more than two groups, and two-tailed *t*-test was used for testing between two groups. Statistical significance is noted as *$p < 0.05$, **$p < 0.01$, ***$p < 0.001$, and ****$p < 0.0001$.

3. Results

3.1. Hemodynamics following HSR in wild-type and *parkin*$^{-/-}$ animals

We evaluated hemodynamics following HSR in both *parkin*$^{+/+}$ and *parkin*$^{-/-}$ mice (9–12w, 25 ± 2.06 g, n = 44) with and without antecedent RIPC. All groups of mice tolerated HSR, as indicated by stable mean arterial pressure (MAP) profiles (Fig. 1A). When RIPC was applied prior to the beginning of the shock protocol, there was a small but significant increase in MAP in both WT and *parkin*$^{-/-}$ animals (Fig. 1B). As illustrated in Fig. 1C, this difference disappeared during the ensuing shock and resuscitation periods and there was no difference among the groups at the end of the experimental period i.e., t = 285 min (Fig. 1C). The volume of blood withdrawn per gram of animal weight (uL/g) was used as an indicator of HSR model standardization and showed no significant differences (Fig. 1D). Hence, *parkin*$^{-/-}$ mice did not have altered hemodynamics compared to WT mice in response to HSR.

3.2. Hepatoprotective and anti-inflammatory effects of RIPC are lost in *parkin*$^{-/-}$ animals

We previously reported that RIPC exerted organ protection in a model of murine HSR (Huang et al., 2011). We suggested that induction of mitophagy by RIPC might contribute to hepatoprotection in this model. *Parkin* is a key protein in the induction of mitophagy. We studied *parkin*$^{-/-}$ animals to understand the role of *parkin* in RIPC-induced hepatoprotection following HSR. As shown in Fig. 2A, RIPC significantly reduces the rise in ALT following HSR (four left bars, $p < 0.001$). By contrast, in the absence of *parkin*, the RIPC-induced protection was no longer observed (four right bars). Histology was performed to evaluate the magnitude of hepatocellular necrosis in each of the experimental groups. As shown in Fig. 2B, HSR caused an increase in hepatocellular necrosis, an effect which was lessened by antecedent RIPC (top eight panels). Consistent with the finding for ALT, HSR also caused an increase in hepatocellular necrosis in *parkin-/-* animals, but the protective effect of RIPC was lost in the absence of *parkin* (lower eight panels). These findings are quantitated in Fig. 2C. We also observed that in the absence of *parkin*, the rise in ALT and the increase in hepatocellular

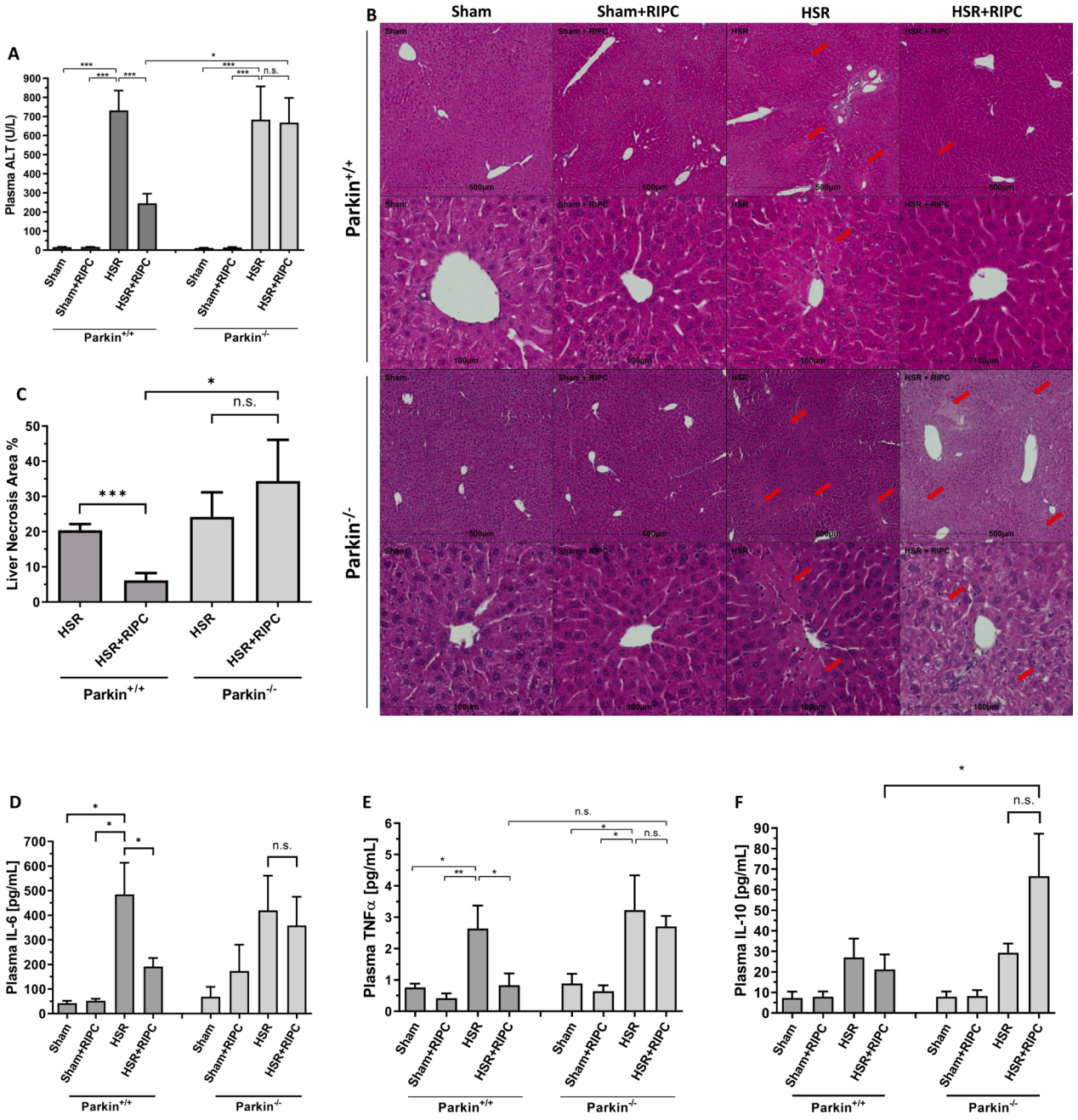

Fig. 2. Hepatoprotective and anti-inflammatory effects of RIPC are lost in *parkin*$^{-/-}$ animals. *(A-C)* Plasma ALT levels were reduced after RIPC in WT *parkin*$^{+/+}$ animals, but not in *parkin*$^{-/-}$ animals, again indicating loss of protection (n = 5–14; ANOVA $p < 0.0001$). Liver H&E staining indicated that necrosis area was reduced following RIPC in HSR WT animals, but not in *parkin*$^{-/-}$ animals (n = 5–6; $p = 0.0380$). Red arrows point to regions of necrosis. Confluent necrosis was defined by areas of the liver that had a marked lighter pink (rather than darker purple) staining; these areas often present with hepatocellular congestion and cytoplasmic vacuolization. *(D-E)* Plasma pro-inflammatory cytokine levels of TNFα (n = 5–6; ANOVA $p = 0.0006$) and IL-6 (n = 5; ANOVA $p = 0.0043$) were increased after HSR, which was reduced after application of RIPC; this protection was lost in *parkin*$^{-/-}$ animals. *(F)* Plasma anti-inflammatory cytokine IL-10 levels were increased after RIPC in HSR *parkin*$^{-/-}$ animals only (n = 5–6; ANOVA $p = 0.0010$). Tukey's: *$p < 0.05$, **$p < 0.01$, ***$p < 0.001$. Mean ± SEM is displayed. n.s. = not significant.

necrosis caused by HSR was comparable to that seen in WT animals. We also measured parameters of systemic inflammation. We evaluated levels of plasma IL-6 and TNF-α (Fig. 2D and 2E respectively). For both, the ability of RIPC to lessen the HSR-induced rise in systemic levels of these cytokines was lost in *parkin*$^{-/-}$ animals. The level of the anti-inflammatory cytokine IL-10 for each treatment group is shown in Fig. 2F. HSR caused a rise in IL-10 levels, an increase which was unaffected by antecedent RIPC in *parkin*$^{+/+}$ mice. Interestingly, in *parkin-/-* animals, the use of RIPC prior to HSR caused a significant rise in IL-10 compared to HSR + RIPC *parkin*$^{+/+}$ mice. RIPC alone did not affect IL-10 levels in wild-type and *parkin*$^{-/-}$ sham animals.

3.3. RIPC augments mitophagy and fission in a parkin-dependent manner in HSR and lessens IRI-induced mitochondrial calcium phosphate granulation

We postulated that mitophagy contributed to the hepatoprotective effect of RIPC following HSR and it did so in a *parkin*-dependent manner. For quantitation, we identified the following ultrastructural morphological features: mitophagophores characterized by counted partially formed double membrane around an elongated mitochondrion (representative shown in Fig. 3A- top left); mitophagosomes fully formed double membrane around a spherical mitochondrion (representative in Fig. 3A- top right); and calcium-phosphate granulation (Fig. 3A- bottom right and left) with dark electron-dense granules within mitochondria. Fig. 3B shows representative TEM micrographs derived from WT and *parkin*$^{-/-}$ animals under each experimental condition. Blinded quantitation of the TEMs is shown in Fig. 3C (for mitophagophores), Fig. 3D (mitophagosomes) and Fig. 3E for calcium phosphate granules. As shown in Fig. 3C and 3D, in WT animals, HSR alone slightly increased both mitophagophore and mitophagosome numbers, however these changes were not significant compared to sham and RIC alone. Importantly, with antecedent RIPC, there was a marked significant rise in both mitophagophores and mitophagosomes compared to other groups ($p < 0.001$). By contrast, in *parkin*$^{-/-}$ animals, the RIPC-induced increase in mitophagophores and mitophagosomes in HSR animals was lost.

Hepatic mitochondrial damage due to IRI can lead to influx and overload of Ca^{2+} which morphologically can present as swelling of the mitochondria and the deposition of calcium-containing, electron dense deposits in the matrix. (Solenski et al., 2002; Dong et al., 2006) These deposits were observed in wild type animals following HSR, but reduced in animals undergoing antecedent RIPC (Fig. 3E). Interestingly, for all experimental groups of *parkin-/-* animals, particularly in the HSR plus RIPC group, the number of these granules increased, suggesting that their clearance, possibly through *parkin*-dependent mechanisms, might be impaired.

To determine whether RIPC changed overall mitochondrial abundance/amount, mitochondrial mass, density, and coverage area were measured in liver tissue. ND1 and ND4 mRNA transcript levels were quantified and normalized to nDNA, as a measure of mitochondrial mass. As shown in Supplementary Fig. 2A and 2B, HSR ± RIPC had no significant effect on ND1 or ND4 copy number in both WT and *parkin*$^{-/-}$ mice. Furthermore, blinded TEM image quantification shows that the density of mitochondria (per 100 μm^2) is unaltered, regardless of *parkin-/-* or HSR ± RIPC (Supplementary Fig. 2C). Mitophagy is a highly dynamic process. To assess whether, at the time point, examined changes in mitophagy resulted in a change in the net mitochondrial mass, we also quantified mitochondrial area coverage percentage (as a surrogate of volume). As shown mitochondrial abundance/amount/mass at the timepoint studied was largely unaltered, despite ultrastructural changes demonstrated in Fig. 3.

RIPC induced significant shifts in mitochondrial population morphology *in vivo*. Hepatic mitochondria can exist on a continuum between spheroids and ovoids, unlike the longer filaments/networks observed in fibroblasts and elsewhere in cell cultures (Youle and van der Bliek, 2012); making them more amenable for morphometric analysis (Willems et al., 2015). As an alternative measure of changes in the morphology of the mitochondrial population, we performed morphometric analysis with a view to better defining size and shape of the mitochondria in the population.

The data are depicted as probability density violin plots (Fig. 4). We evaluated 3 properties of mitochondrial morphology: Fig. 4A shows mitochondrial swelling/ballooning (marked by increased area) and is consistent with hepatocellular injury induced by IRI. Fig. 4B illustrates mitochondrial circularity which is indicative of increased mitophagic fission activity (Westrate et al., 2014; Ding and Yin, 2012; Ke, 2020; Yoo and Jung, 2018). Fig. 4C demonstrates a morphological shift towards less elongated, namely more circular mitochondria, another indicator of mitophagic fission (Westrate et al., 2014; Ding and Yin, 2012; Ke, 2020; Yoo and Jung, 2018).

19,738 individual mitochondria were morphometrically characterized; RIPC and HSR significantly altered overall mitochondrial population morphology. As shown in Fig. 4A, in WT animals, RIPC plus HSR reduced mitochondrial ballooning/swelling compared to HSR alone as depicted by a significant reduction in areas (Fig. 4A). This pattern was lost in *parkin*$^{-/-}$ animals implying that this feature of RIPC is *Parkin*-dependent (Fig. 4A). In WT animals, RIPC induced a shift in the mitochondrial population towards more circular morphologies, while this increase was reversed in *parkin*$^{-/-}$ animals (Fig. 4B). Finally, RIPC in WT HSR animals shifted mitochondria towards less elongated and hence more rounded mitochondria (Fig. 4C) which was reversed in *parkin*$^{-/-}$ animals. This morphometric analysis, evaluating a population-level view of the effect of RIPC on HSR-induced mitochondrial morphologies is consistent with a role for *parkin* in modulating the effect of RIPC on HSR-induced changes in morphology.

As shown in Fig. 3C-D, sham control animals in *parkin*-replete and -deficient mice did not illustrate the presence of mitophagic structures. Therefore, their inclusion in Fig. 4 is not relevant to the discussion around effects of RIPC on mitophagy-favoring morphology. The sham control groups for Fig. 4 are instead included in Supplementary Fig. 4.

3.4. Effect of parkin knockout on other mitophagy receptors

Other mitophagy receptors have been shown to participate in hypoxia-induced mitophagy, including BNIP3L/NIX and FUNDC1. To investigate the possibility that these mitophagy receptors might be reduced in *parkin*$^{-/-}$ animals, and thus account for the reduction in mitophagy in *parkin*$^{-/-}$ animals, we probed for BNIP3L/NIX and FUNDC1 in the liver tissue of untreated animals. As shown in Fig. 5A-5D, the evaluation of protein expression of BNIP3L/NIX and FUNDC1 in the liver tissue of untreated animals showed that *parkin-/-* animals had increased expression of both markers, implying that at baseline, the loss of *Parkin* may be compensated by BNIP3L/NIX and FUNDC1. Similarly, under the various experimental conditions, the expression of these proteins was unaffected in *parkin*$^{-/-}$ animals (Supplemental Fig. 3). Therefore, concomitant reduction in both BNIP3L/NIX and FUNDC1 did not appear to be responsible for reduced mitophagy in *parkin*$^{-/-}$ animals subjected to HSR plus RIPC.

3.5. RIPC alters mitophagy proteins in WT HSR animals

Having shown a central role for *parkin*-dependent mitophagy in the protective effect of RIPC in HSR animals, we assessed liver protein expression of other protein machinery involved in mitophagy. As shown in Fig. 5E and quantitated in Fig. 5F, HSR alone caused a significant rise in *Parkin* protein levels in WT animals; however, this rise was lessened in mice that had undergone antecedent RIPC. To discern whether the effects of RIPC were at the protein or mRNA level, we measured *Parkin* mRNA transcript levels in liver tissue, and found that the changes in *parkin* mRNA levels did not mirror the rise in *parkin* proteins. *Parkin* mRNA levels were less, albeit not significantly, in both the HSR and HSR + RIPC animals ($p = 0.1018$, $n = 4$) (Fig. 5G) compared to treatment

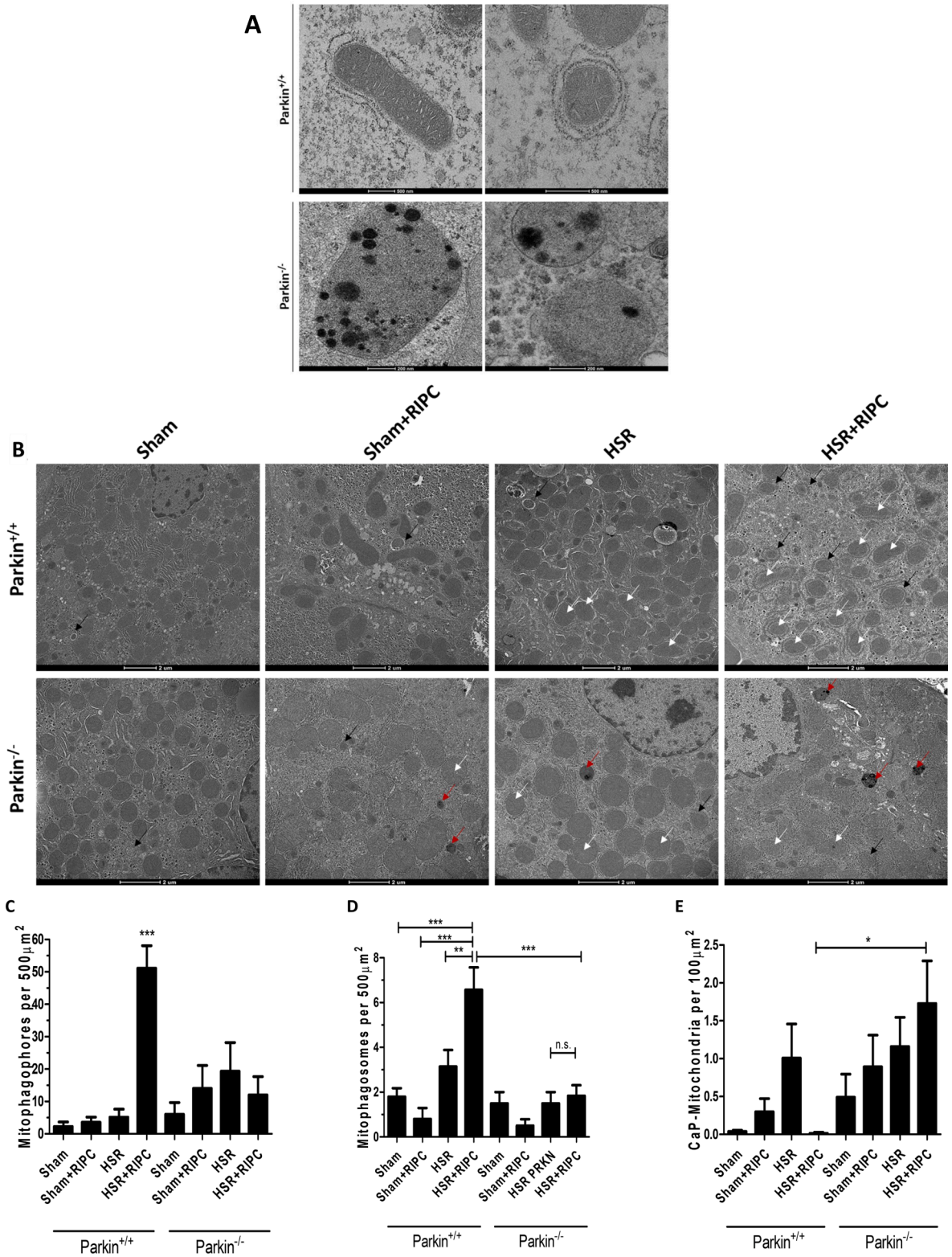

Fig. 3. RIPC augments mitophagy in a *parkin*-dependent manner in HSR and lessens IRI-induced mitochondrial calcium phosphate granulation. (*A*). Transmission electron microscopy images of mitochondria in *parkin*$^{-/-}$ and wild-type animals. Electron micrographs obtained at > 30,000X using the Talos L120C transmission electron microscope system. (*top left*) A partial, double membrane structure forming around an elongated mitochondrion, referred to as a mitophagophore, in WT C57BL/6 mouse liver tissue. (*top right*) A fully formed double-membrane structure formed around a mitochondrion, referred to as a mitophagosome, in WT C57BL/6J mouse liver tissue. (*bottom left and right*) Electron-dense, amorphous, calcium-phosphate granulation of mitochondria within the matrix, in *parkin*$^{-/-}$ mouse liver tissue. Scale bars are located on micrographs. *(B)* Representative transmission electron micrographs (8300X) with black arrows pointing at mitophagosomes, red arrows at calcium phosphate (CaP) granulated mitochondria, and white arrows highlighting mitophagophores. *(C-D)* Blinded quantification of ultrastructures showed that HSR + RIPC WT animals showed more numbers of mitophagosomes (n = 4 per group; ANOVA $p < 0.0001$), and greater numbers of mitophagophores (compared to all other groups) as well (n = 4 per group; ANOVA $p = 0.0004$). *(E) Parkin*$^{-/-}$ animals showed higher numbers of CaP-mitochondria (n = 4–5; ANOVA $p = 0.0136$). Tukey's: *$p < 0.05$, **$p < 0.01$, ***$p < 0.001$. Mean ± SEM is displayed.

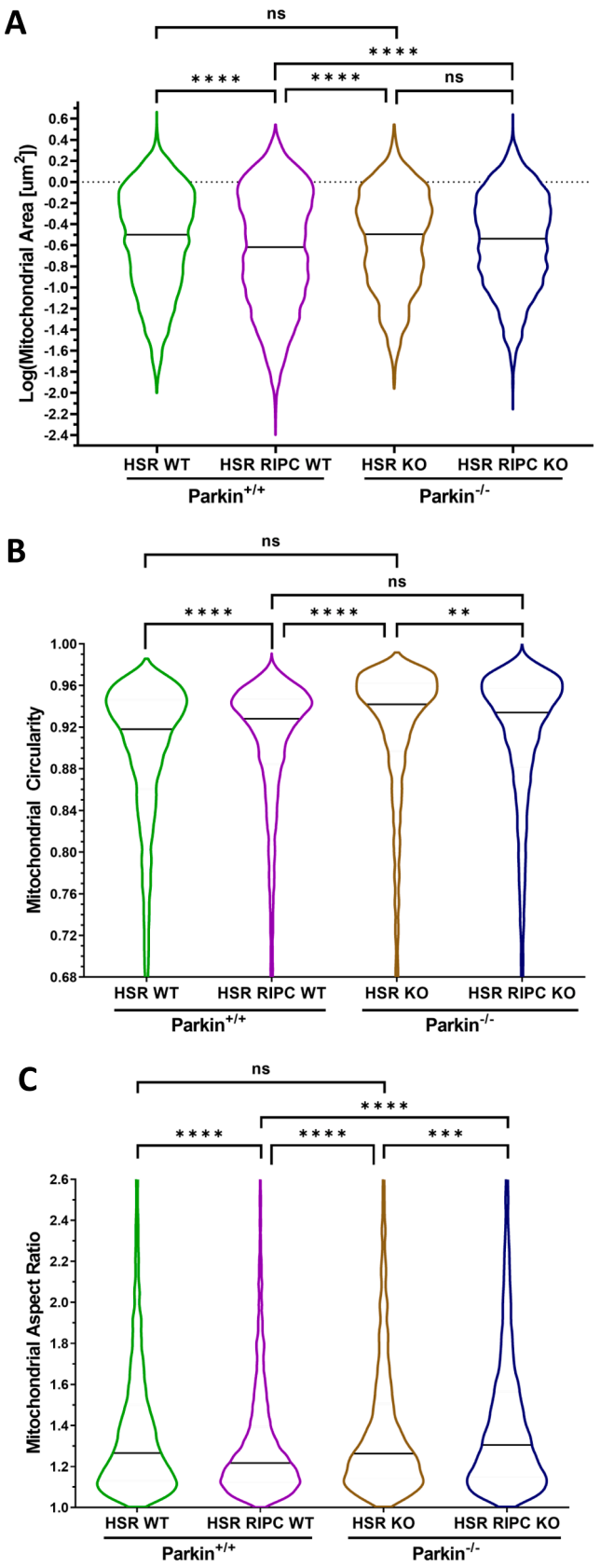

(caption on next column)

Fig. 4. Mitochondrial TEM morphometry showing RIPC inducing fission/mitophagy-favoring morphologies in a *Parkin*-dependent manner in HSR mice. *(A)* RIPC induced a shift in the mitochondrial population towards smaller areas in WT HSR animals but not in *parkin*$^{-/-}$ animals (n = 4–7 mice per group, n = 19,738 mitochondria total; ANOVA p < 2e-16). *(B)* RIPC induced more circular mitochondrial population shift in WT HSR animals but this pattern was reversed in *parkin*$^{-/-}$ animals (n = 4–7 mice per group, n = 19738 mitochondria total; p < 2e-16). *(C)* RIPC induced less elongation (as shown by aspect ratio) in WT HSR animals but this pattern was reversed in *parkin*$^{-/-}$ HSR animals (n = 4–7 mice per group, n = 19,738 mitochondria total; ANOVA p < 2e-16). Data is displayed on probability density violin plots, along with mean lines. Tukey's: *p < 0.05, **p < 0.01, ***p < 0.001, ****p < 0.0001.

controls (Potting et al., 2018; Shires et al., 2020; Alves da Costa et al., 2019).

To further probe the role of other *Parkin*-mediated mitophagy proteins, we evaluated p62 (an adaptor of mitophagy/autophagy) protein expression in liver tissue. As we previously demonstrated (Leung et al., 2018), HSR induced a rise in p62, and antecedent RIPC significantly reduced p62 protein expression in WT animals to levels seen in sham alone (Fig. 5E and quantitated in 5H). However, these changes were not observed in *parkin-/-* animals (Fig. 5E and quantitated in 5H). Finally, we measured the serine/threonine kinase PINK1 protein expression under the various experimental conditions and found that there were no significant changes measured between groups (Fig. 5E and quantitated in 5I), whether performed in WT or *parkin-/-* animals.

4. Discussion

We have previously reported that RIPC applied prior to, or in the early stages of, resuscitated hemorrhagic shock was able to exert an organ protective effect which required the presence of the transcription factor nuclear factor (erythroid-derived 2)-like (Nrf2). In those studies, RIC was shown to increase autophagy in hepatocytes. We suggested that one potential organelle removed was the mitochondrion via the process of mitophagy. Clearance of mitochondria via this process is considered important in maintaining mitochondrial quality, by removing dysfunctional mitochondria known to elaborate cytotoxic reactive oxygen species. In the present studies, we show that RIPC prior to HSR increased mitophagophores and mitophagosomes formation in hepatocytes and skewed mitochondrial morphology to a fission/mitophagy phenotype. These changes were shown to be *parkin*-dependent, in that they disappeared in *parkin*$^{-/-}$ animals. In addition, in the absence of *parkin*, the hepatoprotective effects of antecedent RIPC disappeared. Specifically, the ability of RIPC to lessen HSR-induced rise in liver enzyme release and hepatocellular necrosis, and to reduce the elaboration of the proinflammatory cytokines IL-6 and TNF-α were lost. Together, these findings suggest that RIPC exerted its protection by the induction of *parkin*-dependent mitophagy. One alternate explanation for failure to increase mitophagy in *parkin*$^{-/-}$ animals subjected to RIPC plus HSR is that other key mitophagic proteins might also have been absent in *parkin-/-* animals. We studied two alternate mitophagy adaptor molecules, BNIP3L/NIX and FUNDC1, since both are known to be induced by hypoxia. As shown in Fig. 5A and 5C, both were increased in *parkin-/-* animals compared to WT under baseline conditions and in addition, were modulated following HSR plus RIPC in *parkin-/-* animals compared to WT (Suppl. Fig. 3). Considered together, these findings support the conclusion that an increase in *parkin*-dependent mitophagy induced by HSR plus RIPC contributed to the hepatocellular protection observed seen following the application of RIPC in these animals.

The application of RIPC with HSR caused a profound increase in *parkin*-dependent mitophagy. Activation of upstream signaling pathways represents one possible explanation. Liu and colleague studied intestinal epithelial function following traumatic brain injury and showed that TBI-induced mitophagy occurred via sequential activation of an upstream signaling pathway involving activation of the

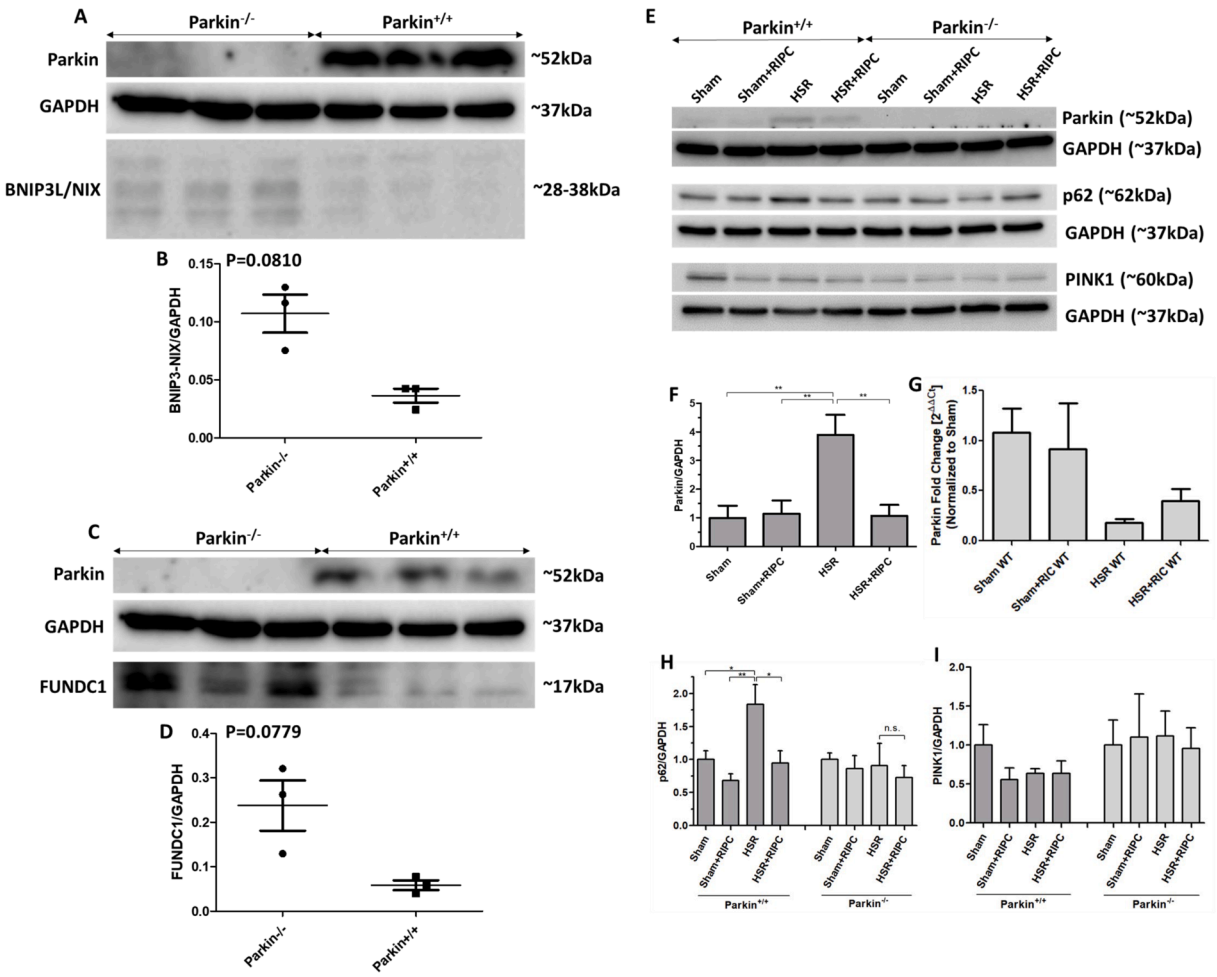

Fig. 5. RIPC alters mitophagy proteins in WT HSR animals in a *Parkin*-dependent manner. *(A-B)* Representative immunoblots, and band densitometry of the mitophagy receptor BNIP3L/NIX shows an increased protein expression in untreated *parkin-/-* animals compared to untreated WT controls (n = 3 mice per group; *t*-test p = 0.081). *(C-D)* Representative immunoblots, and band densitometry of the mitophagy receptor FUNDC1 shows an increased protein expression in untreated *parkin-/-* animals compared to untreated WT controls (n = 3 mice per group; *t*-test p = 0.0779). *(E)* Representative immunoblots for *Parkin*, p62 and PINK1 with GAPDH loading controls for all experimental groups. *(F)* Densitometry quantification showing increased *Parkin* (n = 4–5 mice per group; ANOVA p = 0.003) and *(H)* p62 (n = 5–6 mice per group; ANOVA p = 0.0042) protein levels after induction of HSR, which were reduced after application of RIPC in WT animals but not in *parkin*$^{-/-}$ animals. *(G)* HSR and HSR + RIPC animals showed lower liver *Parkin* mRNA expression compared to Sham controls (n = 4 mice per group; ANOVA p = 0.1018). *(I)* Immunoblots probed for PINK1 (n = 5–6 mice per group; ANOVA p = 0.7641) showed no changes between experimental groups. All signals were normalized to GAPDH loading controls for densitometry quantification and normalized to appropriate sham control mice. Each lane represents liver lysates from unique animals. Tukey's: *p < 0.05, **p < 0.01, ***p < 0.001. Mean ± SEM is displayed.

extracellular signal related kinase (ERK)/Nrf2/heme oxygenase 1 (HO-1). Blockade of ERK lessened downstream Nrf2, HO-1, mitophagy and cellular protection. In addition, mounting evidence suggest that Nrf2 is a regulator of mitochondrial function, quality and energy metabolism (Esteras and Abramov, 2022). Consistent with this as a proposed mechanism, using our HSR model, we previously demonstrated that RIPC plus HSR caused a synergistic increase in ERK1/2, Nrf2 and HO-1 compared to HSR alone, and that blockade of ERK1/2 reduced Nrf2 and HO-1 and obviated hepatoprotection (Leung et al., 2018). This mechanism would also be consistent with the finding that neither Nrf2$^{-/-}$ animals nor *parkin*$^{-/-}$ animals demonstrated the hepatoprotective effects induced by RIPC. Specifically, in both animal strains, the increase in hepatoprotective mitophagy would be lessened. Consistent with this, Kang *et al* recently reported that H_2O_2-induced oxidative stress caused an increase in cellular apoptosis, and increased *parkin*/mitophagy levels and Nrf2 (Kang et al., 2020). Blocking either *parkin*/mitophagy or Nrf2 using knockdown strategies augmented mitochondrial ROS production and cellular apoptosis (Kang et al., 2020). It is also possible that the rise in mitophagy following HSR plus RIPC might have resulted from the recruitment of other mitophagic processes in *parkin*$^{-/-}$ animals. The finding that mitophagy returned to baseline levels in *parkin*$^{-/-}$ animals subjected to HSR plus RIPC makes this unlikely. Finally, while we attribute the hepatoprotection observed following RIPC to the increase in *parkin*-dependent mitophagy, it is attractive to consider that RIPC is hepatoprotective through a cumulative antioxidant effect of the two molecules, namely Nrf2 inducing an antioxidant response in the cell via its effect on the transcription of antioxidant molecules such as heme oxygenase-1, while increased *parkin*-dependent mitophagy rids the cell of dysfunctional oxidant-generating mitochondria. Previously, we have shown a decrease in the ubiquitination of Nrf2 after HSR and an additional reduction in HSR + RIPC animals (Leung et al., 2018). Stemming from this finding, it would be interesting to test if Nrf2 (or Keap1) is a direct substrate of *Parkin* ubiquitination, which could potentially connect the antioxidant system to mitochondrial quality control (MQC) via the UPS, and perhaps establish this functional crosstalk (Itoh et al., 2015).

In the present studies, HSR was shown to increase *Parkin* protein expression, while levels of *parkin* returned to baseline when RIPC was applied prior to HSR. HSR alone was sufficient to induce a rise in *Parkin* protein expression but was not sufficient for the induction of higher

levels of *Parkin*-dependent mitophagy. It was interesting to observe that in animals with HSR plus RIPC, there was a marked rise in mitophagy, which occurred concomitantly with a reduction in *parkin* levels, two findings that may seem contradictory. However, a very plausible explanation is that *parkin* levels are reduced exactly because of the preceding rise in mitophagy. The reduced *parkin* levels in the RIPC plus HSR group may have been a result of the profound increase in mitophagy in this group, resulting in a diminution in *parkin* levels as mitochondria destined for mitophagy, after decoration with ubiquitin, are cleared by the mitophagic process. The process of mitophagy is known to result in the turnover of mitochondrial proteins and potentially of *Parkin* itself (Kovalchuke et al., 2019; Durcan et al., 2014; McLelland et al., 2014). This is also consistent with the findings seen for p62, which increased following HSR, but then fell to control levels in the RIPC plus HSR group. We cannot exclude the possibility that RIPC may promote the degradation of *Parkin* independent of mitophagy, for example via the Ubiquitin-Proteasome System (UPS). For example, in cultured neuronal cells, oxidative stress induced by H_2O_2 was shown to induce *parkin* degradation in a PINK1-dependent pathway involving phospho-ubiquitination of *parkin*.

Mitochondrial network morphology is a tissue and cell-specific parameter, and *in vivo* studies of effects of HSR or ischemia/reperfusion on hepatocyte mitochondrial morphology are limited (Das et al., 2012; Mortiboys et al., 2008; Grünewald et al., 2010; Kalkhoran et al., 2017; Willems et al., 2015; Poole et al., 2008). Using TEM, we showed that RIPC applied in concert with HSR results in increased phagophore-forming ultrastructures. Using ultrastructural morphometry, we found that mitochondrial swelling/ballooning and increased circularity, both observed in HSR animals, were both reversed in animals subjected to HSR plus RIC. In addition, this change in morphology induced by RIPC was not observed in *parkin*$^{-/-}$ animals. This finding is consistent with a less damaged population of mitochondria in RIC animals, dependent on *parkin*-dependent mitophagy. This conclusion is supported by the finding that mitochondria in *parkin*$^{-/-}$ animals exhibited an accumulation of CaP deposits in mitochondria, consistent with an accumulation of depolarized/damaged mitochondria. It is noteworthy that we place the beneficial effect of *parkin* on its ability to contribute to the creation of the mitophagy receptor. However, *Parkin* is also a positive regulator of Drp1-dependent fission (Lutz et al., 2009; Buhlman et al., 2014), and therefore might be promoting changes in mitochondrial morphology, such that it is more amenable to mitophagic processes. Taken together, our data support a model where RIPC promotes mitochondrial quality through *Parkin*-dependent mitophagy (Buhlman et al., 2014; Cereghetti et al., 2008).

The present studies elucidate the mechanisms whereby remote ischemic preconditioning can exert hepatocellular protection in a model of murine hemorrhagic shock-resuscitation. The data clearly point to the ability of RIC to promote *parkin*-dependent mitophagy as being central to the beneficial effects. While RIC is a safe and readily performed intervention, the work also suggests that, in the setting of ischemia–reperfusion, strategies aimed at optimizing mitochondrial quality through enhancing mitophagic clearance of dysfunctional mitochondria may represent a broader approach to mitigating cellular and hence organ injury. Understanding the details of the mitophagic process and its regulation will be essential to capitalize on this approach.

Disclosures:

The authors have no conflicts of interest to disclose.

Funding:

This work was funded by grants from the Canadian Institutes of Health Research #23766. ANM was supported by funds from the St. Michael's Hospital Foundation and the Institute of Medical Science, University of Toronto.

Declaration of Competing Interest

The authors declare that they have no known competing financial interests or personal relationships that could have appeared to influence the work reported in this paper.

Acknowledgements

The authors would like to thank Yan Chen and Lindsey Fiddes, PhD from the Microscopy Imaging Laboratory at the Faculty of Medicine, University of Toronto for transmission electron microscopy ultrathin microtomy and imaging technical support, respectively. The authors would like to thank Xiaofeng Lu, Caterina Di Ciano-Oliveira, PhD and Pamela Plant, PhD from the Research Core Facilities at the Keenan Research Centre for Biomedical Science for technical/methodological expertise in histology, microscopy, and molecular biology, respectively.

Appendix A. Supplementary material

Supplementary data to this article can be found online at https://doi.org/10.1016/j.mito.2023.03.002.

References

Alves da Costa, C., Duplan, E., Rouland, L., Checler, F., 2019. The transcription factor function of Parkin: breaking the dogma. Front. Neurosci. 12, 965.
Buhlman, L., Damiano, M., Bertolin, G., et al., 2014. Functional interplay between Parkin and Drp1 in mitochondrial fission and clearance. BBA 1843 (9), 2012–2026.
Cereghetti, G.M., Stangherlin, A., de Brito, O.M., et al., 2008. Dephosphorylation by calcineurin regulates translocation of Drp1 to mitochondria. Proc. Natl. Acad. Sci. 105 (41), 15803–15808.
Chen, C.H., Liu, K., Chan, J.Y.H., 2008. Anesthetic preconditioning confers acute cardioprotection via UP-regulation of manganese superoxide dismutase and preservation of mitochondrial respiratory enzyme activity. Shock (Augusta, Ga). 29 (2), 300–308.
Cheung, M.M., Kharbanda, R.K., Konstantinov, I.E., et al., 2006. Randomized controlled trial of the effects of remote ischemic preconditioning on children undergoing cardiac surgery: first clinical application in humans. J. Am. Coll. Cardiol. 47 (11), 2277–2282.
Coronado, M., Fajardo, G., Nguyen, K., et al., 2018. Physiological mitochondrial fragmentation is a normal cardiac adaptation to increased energy demand. Circ. Res. 122 (2), 282–295.
Das, S., Hajnóczky, N., Antony, A.N., et al., 2012. Mitochondrial morphology and dynamics in hepatocytes from normal and ethanol-fed rats. Pflugers Arch. 464 (1), 101–109.
Davidson, G.H., Hamlat, C.A., Rivara, F.P., Koepsell, T.D., Jurkovich, G.J., Arbabi, S., 2011. Long-term survival of adult trauma patients. JAMA 305 (10), 1001–1007.
De Gaetano, A., Gibellini, L., Bianchini, E., et al., 2020. Impaired mitochondrial morphology and functionality in Lonp1(wt/-) mice. J Clin Med. 9 (6), 1783.
Ding, W.-X., Yin, X.-M., 2012. Mitophagy: mechanisms, pathophysiological roles, and analysis. Biol. Chem. 393 (7), 547–564.
Dong, Z., Saikumar, P., Weinberg, J.M., Venkatachalam, M.A., 2006. Calcium in cell injury and death. Annu. Rev. Pathol. 1, 405–434.
Durcan, T.M., Tang, M.Y., Pérusse, J.R., et al., 2014. USP8 regulates mitophagy by removing K6-linked ubiquitin conjugates from parkin. EMBO J. 33 (21), 2473–2491.
Esteras, N., Abramov, A.Y., 2022. Nrf2 as a regulator of mitochondrial function: Energy metabolism and beyond. Free Radic. Biol. Med.
Garvin, A.M., Aurigemma, N.C., Hackenberger, J.L., Korzick, D.H., 2017. Age and ischemia differentially impact mitochondrial ultrastructure and function in a novel model of age-associated estrogen deficiency in the female rat heart. Pflugers Arch. 469 (12), 1591–1602.
Go, K.L., Lee, S., Zendejas, I., Behrns, K.E., Kim, J.S., 2015. Mitochondrial dysfunction and autophagy in hepatic ischemia/reperfusion injury. Biomed Res. Int. 2015, 183469.
Goldberg, M.S., Fleming, S.M., Palacino, J.J., et al., 2003. Parkin-deficient mice exhibit nigrostriatal deficits but not loss of dopaminergic neurons. J. Biol. Chem. 278 (44), 43628–43635.
Grünewald, A., Voges, L., Rakovic, A., et al., 2010. Mutant Parkin impairs mitochondrial function and morphology in human fibroblasts. PLoS One 5 (9), e12962.
Gu, J., Zhang, T., Guo, J., Chen, K., Li, H., Wang, J., 2020. PINK1 Activation and translocation to mitochondria-associated membranes mediates mitophagy and protects against hepatic ischemia/reperfusion injury. Shock (Augusta, Ga). 54 (6), 783–793.
Hougaard, K.D., Hjort, N., Zeidler, D., et al., 2013. Remote ischemic perconditioning in thrombolysed stroke patients: randomized study of activating endogenous neuroprotection - design and MRI measurements. Int. J. Stroke: Off. J. Int. Stroke Soc. 8 (2), 141–146.
Huang, C., Andres, A.M., Ratliff, E.P., Hernandez, G., Lee, P., Gottlieb, R.A., 2011. Preconditioning involves selective mitophagy mediated by Parkin and p62/SQSTM1. PLoS One 6 (6), e20975.
Itoh, K., Ye, P., Matsumiya, T., Tanji, K., Ozaki, T., 2015. Emerging functional cross-talk between the Keap1-Nrf2 system and mitochondria. J. Clin. Biochem. Nutr. 56 (2), 91–97.

Kalkhoran, S.B., Munro, P., Qiao, F., et al., 2017. Unique morphological characteristics of mitochondrial subtypes in the heart: the effect of ischemia and ischemic preconditioning. Discoveries 5.
Kalogeris, T., Baines, C.P., Krenz, M., Korthuis, R.J., 2012. Cell biology of ischemia/reperfusion injury. Int. Rev. Cell Mol. Biol. 298, 229–317.
Kang, L., Liu, S., Li, J., Tian, Y., Xue, Y., Liu, X., 2020. Parkin and Nrf2 prevent oxidative stress-induced apoptosis in intervertebral endplate chondrocytes via inducing mitophagy and anti-oxidant defenses. Life Sci. 243, 117244.
Ke, P.-Y., 2020. Mitophagy in the pathogenesis of liver diseases. Cells 9 (4), 831.
Khraiwesh, H., López-Domínguez, J.A., López-Lluch, G., et al., 2013. Alterations of ultrastructural and fission/fusion markers in hepatocyte mitochondria from mice following calorie restriction with different dietary fats. J. Gerontol.: A 68 (9), 1023–1034.
Kim, J.S., He, L., Qian, T., Lemasters, J.J., 2003. Role of the mitochondrial permeability transition in apoptotic and necrotic death after ischemia/reperfusion injury to hepatocytes. Curr Mol Med. 3 (6), 527–535.
Kim, I., Rodriguez-Enriquez, S., Lemasters, J.J., 2007. Selective degradation of mitochondria by mitophagy. Arch. Biochem. Biophys. 462 (2), 245–253.
Koch, C., Chaudru, S., Lederlin, M., Jaquinandi, V., Kaladji, A., Mahé, G., 2016. Remote ischemic preconditioning and contrast-induced nephropathy: a systematic review. Ann. Vasc. Surg. 32, 176–187.
Kong, W.N., Li, W., Bai, C., Dong, Y., Wu, Y., An, W., 2021. Augmenter of liver regeneration-mediated mitophagy protects against hepatic ischemia/reperfusion injury. Am. J. Transpl.: Off. J. Am. Soc. Transpl. Am. Soc. Transpl. Surg.
Kovalchuke, L., Mosharov, E.V., Levy, O.A., Greene, L.A., 2019. Stress-induced phospho-ubiquitin formation causes parkin degradation. Sci. Rep. 9 (1), 11682.
Leung, C.H., Caldarone, C.A., Wang, F., et al., 2015. Remote ischemic conditioning prevents lung and liver injury after hemorrhagic shock/resuscitation: potential role of a humoral plasma factor. Ann. Surg. 261 (6), 1215–1225.
Leung, C.H., Caldarone, C.A., Guan, R., et al., 2018. Nrf2 Regulates the hepatoprotective effects of remote ischemic conditioning in hemorrhagic shock. Antioxid. Redox Signal.
Li, C., Li, Y.S., Xu, M., et al., 2013. Limb remote ischemic preconditioning for intestinal and pulmonary protection during elective open infrarenal abdominal aortic aneurysm repair: a randomized controlled trial. Anesthesiology 118 (4), 842–852.
Li, N., Wang, H., Jiang, C., Zhang, M., 2018. Renal ischemia/reperfusion-induced mitophagy protects against renal dysfunction via Drp1-dependent-pathway. Exp. Cell Res. 369 (1), 27–33.
Lim, S.Y., Hausenloy, D.J., 2012. Remote ischemic conditioning: from bench to bedside. Front. Physiol. 3, 27.
Livingston, M.J., Wang, J., Zhou, J., et al., 2019. Clearance of damaged mitochondria via mitophagy is important to the protective effect of ischemic preconditioning in kidneys. Autophagy 15 (12), 2142–2162.
Lucocq, J.M., Hacker, C., 2013. Cutting a fine figure: on the use of thin sections in electron microscopy to quantify autophagy. Autophagy 9 (9), 1443–1448.
Lutz, A.K., Exner, N., Fett, M.E., et al., 2009. Loss of parkin or PINK1 function increases Drp1-dependent mitochondrial fragmentation. J. Biol. Chem. 284 (34), 22938–22951.
McLelland, G.L., Soubannier, V., Chen, C.X., McBride, H.M., Fon, E.A., 2014. Parkin and PINK1 function in a vesicular trafficking pathway regulating mitochondrial quality control. EMBO J. 33 (4), 282–295.
Mekada, K., Yoshiki, A., 2021. Substrains matter in phenotyping of C57BL/6 mice. Exp. Anim. 70 (2), 145–160. https://doi.org/10.1538/expanim.20-0158.
Mollica, M.P., Mattace Raso, G., Cavaliere, G., et al., 2017. Butyrate regulates liver mitochondrial function, efficiency, and dynamics in insulin-resistant obese mice. Diabetes 66 (5), 1405–1418.
Mortiboys, H., Thomas, K.J., Koopman, W.J., et al., 2008. Mitochondrial function and morphology are impaired in parkin-mutant fibroblasts. Ann. Neurol. 64 (5), 555–565.
Pinto, M., Nissanka, N., Moraes, C.T., 2018. Lack of Parkin anticipates the phenotype and affects mitochondrial morphology and mtDNA levels in a mouse model of Parkinson's disease. J. Neurosci. 38 (4), 1042–1053.
Poole, A.C., Thomas, R.E., Andrews, L.A., McBride, H.M., Whitworth, A.J., Pallanck, L.J., 2008. The PINK1/Parkin pathway regulates mitochondrial morphology. Proc. Natl. Acad. Sci. 105 (5), 1638–1643.
Potting, C., Crochemore, C., Moretti, F., et al., 2018. Genome-wide CRISPR screen for PARKIN regulators reveals transcriptional repression as a determinant of mitophagy. Proc. Natl. Acad. Sci. USA 115 (2), E180–e189.
Quarrie, R., Lee, D.S., Steinbaugh, G., et al., 2012. Ischemic preconditioning preserves mitochondrial membrane potential and limits reactive oxygen species production. J. Surg. Res. 178 (1), 8–17.
Redmann, M., Benavides, G.A., Wani, W.Y., et al., 2018. Methods for assessing mitochondrial quality control mechanisms and cellular consequences in cell culture. Redox Biol. 17, 59–69.
Regel, G., Grotz, M., Weltner, T., Sturm, J.A., Tscherne, H., 1996. Pattern of organ failure following severe trauma. WORLD J. Surg. 20 (4), 422–429.
Reis-Barbosa, P.H., de-Carvalho, J.J., del Sol, M., Mandarim-de-Lacerda, C.A., 2020. Commentary on mitochondrial stereology in transmission electron microscopy. Int. J. Morphol. 38, 26–29.
Shires, S.E., Quiles, J.M., Najor, R.H., et al., 2020. Nuclear Parkin activates the ERRα transcriptional program and drives widespread changes in gene expression following hypoxia. Sci. Rep. 10 (1), 8499.
Slagsvold, K.H., Rognmo, Ø., Høydal, M., Wisløff, U., Wahba, A., 2014. Remote ischemic preconditioning preserves mitochondrial function and influences myocardial MicroRNA expression in atrial myocardium during coronary bypass surgery. Circ. Res. 114 (5), 851–859.
Solenski, N.J., diPierro, C.G., Trimmer, P.A., Kwan, A.L., Helm, G.A., 2002. Ultrastructural changes of neuronal mitochondria after transient and permanent cerebral ischemia. Stroke 33 (3), 816–824.
Turrell, H.E., Thaitirarot, C., Crumbie, H., Rodrigo, G., 2014. Remote ischemic preconditioning of cardiomyocytes inhibits the mitochondrial permeability transition pore independently of reduced calcium-loading or sarcKATP channel activation. Physiol Rep. 2 (11), e12231.
Velez, D.E., Hermann, R., Barreda Frank, M., et al., 2016. Effects of wortmannin on cardioprotection exerted by ischemic preconditioning in rat hearts subjected to ischemia-reperfusion. J. Physiol. Biochem. 72 (1), 83–91.
Venegas, V., Halberg, M.C., 2012. Measurement of mitochondrial DNA copy number. Methods Mol. Biol. (Clifton, NJ). 837, 327–335.
Wang, Y., Shen, J., Xiong, X., et al., 2014. Remote ischemic preconditioning protects against liver ischemia-reperfusion injury via heme oxygenase-1-induced autophagy. PLoS One 9 (6), e98834.
Westermann, B., 2012. Bioenergetic role of mitochondrial fusion and fission. BBA 1817 (10), 1833–1838.
Westrate, L.M., Drocco, J.A., Martin, K.R., Hlavacek, W.S., MacKeigan, J.P., 2014. Mitochondrial morphological features are associated with fission and fusion events. PLoS One 9 (4), e95265.
Willems, P.H., Rossignol, R., Dieteren, C.E., Murphy, M.P., Koopman, W.J., 2015. Redox homeostasis and mitochondrial dynamics. Cell Metab. 22 (2), 207–218.
Wu, M.Y., Yiang, G.T., Liao, W.T., et al., 2018. Current mechanistic concepts in ischemia and reperfusion injury. Cell. Physiol. Biochem. 46 (4), 1650–1667.
Yoo, S.M., Jung, Y.K., 2018. A molecular approach to mitophagy and mitochondrial dynamics. Mol. Cells 41 (1), 18–26.
Youle, R.J., van der Bliek, A.M., 2012. Mitochondrial fission, fusion, and stress. Science (New York, N.Y.) 337 (6098), 1062–1065.
Yu, S., Zheng, S., Leng, J., Wang, S., Zhao, T., Liu, J., 2016. Inhibition of mitochondrial calcium uniporter protects neurocytes from ischemia/reperfusion injury via the inhibition of excessive mitophagy. Neurosci. Lett. 628, 24–29.
Zhang, H., Yan, Q., Wang, X., et al., 2021. The role of mitochondria in liver ischemia-reperfusion injury: from aspects of mitochondrial oxidative stress, mitochondrial fission, mitochondrial membrane permeable transport pore formation, mitophagy, and mitochondria-related protective measures. Oxid. Med. Cell. Longev. 2021, 6670579.
Zheng, X., Zu, L., Becker, L., Cai, Z.P., 2014. Ischemic preconditioning inhibits mitochondrial permeability transition pore opening through the PTEN/PDE4 signaling pathway. Cardiology 129 (3), 163–173.
Zhu, D.J., Liao, X.H., Huang, W.Q., Sun, H., Zhang, L., Liu, Q., 2020. Augmenter of liver regeneration protects renal tubular epithelial cells from ischemia-reperfusion injury by promoting PINK1/Parkin-mediated mitophagy. Front. Physiol. 11, 178.